Changes in non-dipolar field structure over the Plio-Pleistocene: New paleointensity results from Hawai‘i compared to global datasets

Brendan Cych[1], Lisa Tauxe[1], Geoffrey Cromwell[2], John Sinton[3], and Anthony Koppers[4]

[1]UC San Diego
[2]U.S. Geological Survey
[3]University of Hawai'i
[4]Oregon State University,Oregon State University

May 22, 2023

Changes in non-dipolar field structure over the Plio-Pleistocene: New paleointensity results from Hawaiʻi compared to global datasets

Brendan Cych [1,5], Lisa Tauxe [1], Geoffrey Cromwell [2,6], John Sinton [3], Anthony A.P. Koppers [4]

[1]University of California, San Diego, CA, USA
[2]Occidental College, Los Angeles, CA, USA
[3]University of Hawaiʻi at Manōa, HI, USA
[4]Oregon State University, Corvallis, OR, USA
[5]Now at University of Liverpool, UK
[6]Now at US Geological Survey, California Water Science Center, Santa Maria, CA, USA

Key Points:

- Global compilations of paleointensity do not conform with the hypothesis that Earth's time-averaged magnetic field is a dipole (GAD field)
- We present 31 new paleointensity results from 0-4 Ma from the Hawaiian Islands
- Results for 0-1.5 Ma are inconsistent with a GAD field when compared to global datasets reanalyzed the same way, but are consistent for 1.5 to 2.5 Ma

Corresponding author: Brendan Cych, `bcych@liverpool.ac.uk`

Abstract

A foundational assumption in paleomagnetism is that the Earth's magnetic field behaves as a geocentric axial dipole (GAD) when averaged over sufficient timescales. Compilations of directional data averaged over the past 5 Ma yield a distribution largely compatible with GAD, but the distribution of paleointensity data over this timescale is incompatible. Reasons for the failure of GAD include: 1) Arbitrary "selection criteria" to eliminate "unreliable" data vary among studies, so the paleointensity database may include biased results. 2) The age distribution of existing paleointensity data varies with latitude, so different latitudinal averages represent different time periods. 3) The time-averaged field could be truly non-dipolar.

Here, we present a consistent methodology for analyzing paleointensity results and comparing time-averaged paleointensities from different studies. We apply it to data from Plio/Pleistocene Hawai'ian igneous rocks, sampled from fine-grained, quickly cooled material (lava flow tops, dike margins and scoria cones) and subjected to the IZZI-Thellier technique; the data were analyzed using the BiCEP method of Cych et al (2021, doi:10.1029/2021GC009755), which produces accurate paleointensity estimates without arbitrarily excluding specimens from the analysis. We constructed a paleointensity curve for Hawai'i over the Plio/Pleistocene using the method of Livermore et al (2018, doi:10.1093/gji/ggy383), which accounts for the age distribution of data. We demonstrate that even with the large uncertainties associated with obtaining a mean field from temporally sparse data, our average paleointensities obtained from Hawai'i and Antarctica (reanalyzed from Asefaw et al., 2021, doi:10.1029/2020JB020834) are not GAD-like from 0 - 1.5 Ma but may be prior to that.

Plain Language Summary

Paleomagnetists make the assumption that the Earth's magnetic field behaves like a bar magnet centered at the spin axis, known as a Geocentric Axial dipole or GAD. Compilations of the magnetic field's direction are largely consistent with this assumption, but compilations of its strength (paleointensity) are not. A number of causes for this could be: 1) The different experimental methods and the criteria used to pass or exclude paleointensity data might cause differences in records. 2) The ages of records differ between locations. 3) The field really doesn't behave like a bar magnet. To test this, we performed paleointensity experiments on rocks collected in Hawai'i and compared our results to results of similar age from other locations analyzed using the same methodology. The three locations analyzed in this study do not produce time-averaged paleointensities consistent with a GAD field for the most recent 1.5 million years, but a GAD field cannot be ruled out before this time. This indicates that differences in time-averaged field strength in global records can be unrelated to differences in methodology or age between studies.

1 Introduction

Paleomagnetists use the direction of the magnetization acquired in the Earth's ancient magnetic field to obtain estimates of the ancient latitude at which the rock formed. Calculation of a latitude relies on the assumption that the Earth's magnetic field is structured like a bar magnet when averaged over sufficiently long timescales, so that the magnetic field is vertical at the poles, and horizontal at the equator, also termed a Geocentric Axial Dipole (GAD). Estimates of the Earth's magnetic field direction, taken from different latitudes over the past 10 Ma conform relatively well to a GAD field, with a small hemispheric asymmetry (Cromwell et al., 2018). On the other hand, estimates of the Earth's magnetic field strength (the paleointensity) averaged over the last 5 Ma consistently show a behaviour incompatible with a strongly dipolar field. A seemingly persistent feature in paleointensity data is the presence of weak paleofields at high southern latitudes (Lawrence et al., 2009; Asefaw et al., 2021; Tauxe et al., 2022), which causes a hemispheric asymmetry in the paleointensity data. This is seen in paleointensities from the MagIC database over the last 5 Ma (plotted in Figure 1a) where the mean paleointensity at 80°S would be produced by a centered magnetic dipole with a moment of around 40 ZAm^2, whereas the mean paleointensity at 20°N would require a dipole moment with a magnitude closer to 80 ZAm^2. Attempts to fit Giant Gaussian Process (GGP) models to paleointensity data to determine the structure of the time-averaged field have found that the field consistently requires a strong quadrupole term 15-30% the strength of the dipole field (Muxworthy, 2017; Shcherbakov et al., 2019), producing this asymmetry. However, such a large quadrupole is completely incompatible with the directional data.

Three different hypotheses could explain the non-dipole like behaviour of global time-averaged paleointensity records: bias in paleointensity estimation, comparison of temporally distinct data in a time-varying field, and genuine non-dipole field behavior. Regarding the issue of bias, paleointensity estimation involves normalizing the observed natural remanent magnetization (NRM) to a magnetization acquired in a known laboratory field. The accurate determination of a paleointensity therefore requires that the acquisition of a magnetization be reproducible in the laboratory. However, it has been shown (e.g., Levi, 1977; Dunlop & Özdemir, 2001; Krása et al., 2003; Tauxe et al., 2021) that some rocks have non-reproducible magnetizations, which can lead to biased paleointensity estimates. Global paleointensity records may be confounded by these biased estimates, leading to an apparent non-dipole signature. Alternatively, geomagnetic intensity variations through time may not be well averaged. The majority of paleointensity determinations are made with volcanic rocks, which record an instantaneous snapshot of the magnetic field at the time they cool. Archeomagnetic data indicate that the Earth's magnetic field strength can vary strongly over decades to centuries (e.g., Shaar et al., 2020), so numerous paleointensity estimates are necessary for a good average. If the field strength varies over long timescales (e.g., millions of years), then comparing the "average" of two studies may not be meaningful if the units sampled are of different ages. And finally, it is also possible that the geomagnetic field is not in fact GAD-like but has long-term non-axial dipole contributions (as suggested by Wilson, 1970; Cromwell et al., 2013; Tauxe et al., 2022).

Paleomagnetists have identified behaviors in a paleointensity experiment that deviate from theoretical expectations and may lead to bias and recent studies have made a greater effort to eliminate such biased results. In most paleointensity studies, results from paleomagnetic specimens are excluded from the analysis if they fail a set of "selection criteria" which are phenomenological descriptions of these behaviors. Alternatively, the BiCEP method (Cych et al., 2021) attempts to find a relationship between the apparent paleointensity and one of these commonly used selection criteria (curvature, Paterson, 2011), and attempts to correct for the bias induced by the non-ideal behavior, obtaining accurate results without excluding data from the analysis based on arbitrary criteria. Recently, a study (Tauxe et al., 2022) which used the strict CCRIT criteria (Cromwell et al., 2015) and the BiCEP method on paleointensity studies from several latitudes found that there is still a discrepancy between these time-averaged paleointensities and those expected for a GAD field, making our first hypothesis (apparent non-dipole behavior is caused by bias in paleointensity estimation) unlikely to be the cause of inaccurate paleointensities.

Figure 1b shows the age distribution of latitudinally binned absolute paleointensity data in the MagIC database (without selection). It is apparent that different latitude bins have different age distributions. Because of this, the average paleointensity from each bin is representative of a different time period, and is not an average paleointensity for the whole of the last 5 Ma. High quality paleointensity data, analyzed in a consistent manner, are needed to determine whether temporal sampling is the cause of

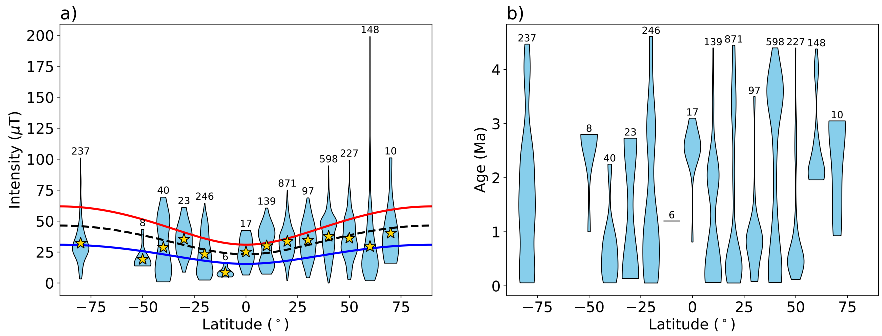

Figure 1. Violin plots showing latitudinal binned distributions of a) paleointensity and b) age for reported paleointensity results from the MagIC database aged between 50 ka and 5 Ma. In a violin plot, the width of the violin represents the frequency of intensities in that latitude bin, with the widest point in the violin representing the modal value. The number of data points in each bin are noted above the violins. The yellow stars in a) are the mean paleointensity value at each latitude bin and the solid blue, dashed black and solid red lines represent the expected mean values for a dipole field with a strength of 40, 60 and 80 ZAm^2 respectively.

apparent non-dipolar behavior, or if the time-averaged field is truly non-dipolar, as outlined in our third hypothesis.

In this paper, we present paleointensity estimates from rapidly cooled volcanic material from lava flows, dikes and vent deposits (scoria and spatter cones) aged 0-4 Ma from the Hawai‘ian islands. In Section 2, we describe how we collect samples in the field (2.1), how we conduct paleointensity experiments (2.2) on specimens therefrom, how we analyze our results using the BiCEP method which produces accurate estimates for specimens magnetized in known fields (2.3), and how we obtain ages for our samples using ^{40}Ar/^{39}Ar dating (2.4). In Section 3, we show the results of our paleointensity study in Hawai‘i. We provide a discussion of the disadvantages of traditional methods of paleointensity selection in Section 4.1. Section 4.2 discusses how our results suggest that scoria may be a useful lithology for obtaining high-quality paleointensity estimates, and are in agreement with estimates from other lithologies. In Section 4.3 we fit a model to our results in an attempt to derive a time average that accounts for uneven temporal sampling. We then apply the same methodology to studies from Northern Israel and Antarctica which targeted similar materials. This allows us to test whether poor temporal sampling or non-dipole behavior is responsible for the weaker paleointensity at high latitudes. Our results indicate that there is a persistent non-dipole component in the Earth's magnetic field over at least the past 1.5 Ma with older data being much more consistent with a GAD field.

2 Methods

2.1 Field Methods

Our results come from samples collected over three field seasons from outcrops on the Hawai‘ian islands. Samples were collected from the islands of Hawai‘i, Maui, Moloka‘i, and O‘ahu in an attempt to get a representative average paleointensity over the past 4 Ma. This study targeted predominantly glassy and fine grained igneous material from lava flow tops and bottoms, scoria cones and dike margins. Néel theory (Néel, 1949) predicts the physics of "uniaxial single domain" grains which should behave ideally in a pa-

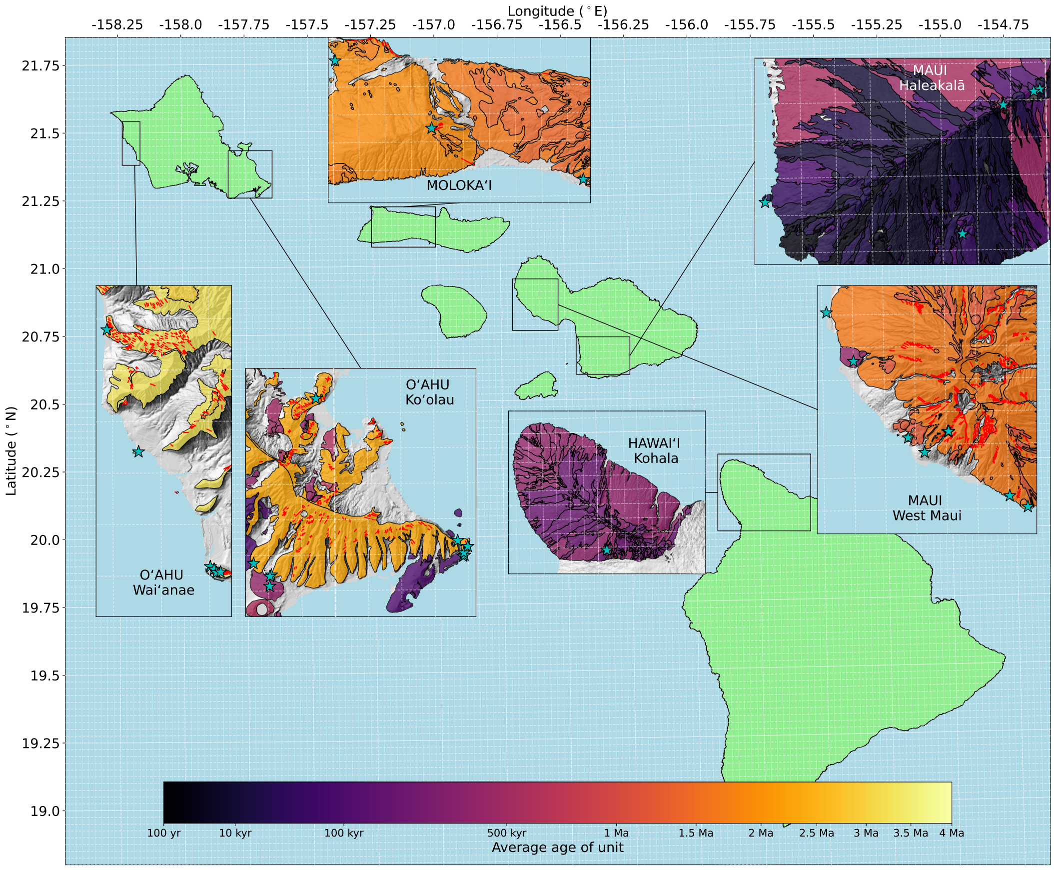

Figure 2. Maps showing sampling localities for successful sites used in this study (blue stars). Insets are labeled with the name of each island in capital letters and the name of the volcano (if applicable) in lowercase. Each map shows samples from a different Volcano/Island. Colors represent ages of units (Sherrod et al., 2007), with darker colors indicating younger flows (see colorbar), and dike locations indicated by red lines. Topographic data: U.S. Geological Survey (USGS). 2015. USGS 10-m Digital Elevation Model (DEM): Hawai'i. Coastline data: Hawai'i Statewide GIS Program.

leointensity experiment. Only very small magnetic particles exhibit single-domain behavior, and so we sampled rapidly cooled materials most likely to contain these fine grains.

In the field, we collected small unoriented hand samples using a hammer and chisel; this allowed us to obtain smaller pieces of material and was less destructive than obtaining oriented specimens with a drill. Maps of our sampling localities are shown in Figure 2 and details regarding location, age and material are given in Table 1.

2.2 Laboratory Work

Each sample was crushed with a mortar and pestle to produce multiple paleomagnetic specimens with masses on the order of 0.1 g. Specimens were weighed and glued into 1 cm wide borosilicate glass tubes using a high temperature, low magnetic moment glue (KaSil). We subjected each specimen to the IZZI-Thellier method (Tauxe & Staudigel, 2004; Yu et al., 2004). This is a step-wise double heating experiment in which the NRM is replaced by a Thermal Remanent Magnetization (TRM) acquired in a known

Table 1. Ages and locations for sites from this study that passed CCRIT or BiCEP. Locations for all sites, including those that did not pass CCRIT or BiCEP are listed in the supporting information. Latitudes and Longitudes are referenced to the WGS84 standard. Codes in the methods column represent the method or citation used. AP: Ar-Ar age plateau, II: Ar-Ar inverse isochron, MP: Ar-Ar mini-plateau, O05: K-Ar age (Ozawa et al., 2005), S03: K-Ar age/stratigraphic relationship (Sherrod et al., 2007), SR: Stratigraphic relationships with other dated units (Sherrod et al., 2007), T03: K-Ar age (Tagami et al., 2003), TF: Ar-Ar Total Fusion Age. For more detailed explanation, see Section 2.4

Site	Island	Lithology	Lat. (°Ṅ)	Lon. (°E)	Age (Ma)	$\pm 2\sigma$	Method
HW306	Hawai'i	Vent Deposit	20.04470	-155.73437	0.1900	0.0700	SR
ML001	Moloka'i	Dike	21.13719	-157.15547	2.0700	0.0200	TF
ML012	Moloka'i	Vent Deposit	21.08955	-157.01053	1.6100	0.0300	AP
ML015	Moloka'i	Vent Deposit	21.19876	-157.24734	1.7700	0.0200	AP
MU004	Maui	Vent Deposit	20.77605	-156.53433	1.4300	0.0200	AP
MU009	Maui	Vent Deposit	20.81885	-156.61782	0.6100	0.0120	T03
MU011	Maui	Vent Deposit	20.83016	-156.63110	1.2300	0.0690	II
MU012	Maui	Vent Deposit	20.88931	-156.67484	0.3000	0.0216	AP
MU013	Maui	Vent Deposit	20.92685	-156.69633	0.5840	0.0100	T03
MU023	Maui	Vent Deposit	20.61085	-156.31100	0.0765	0.0635	S03
MU025	Maui	Vent Deposit	20.70692	-156.25424	0.0950	0.0450	S03
MU027	Maui	Vent Deposit	20.70551	-156.25857	0.0950	0.0450	S03
MU031	Maui	Vent Deposit	20.69669	-156.28040	0.0670	0.0404	AP
MU036	Maui	Vent Deposit	20.63397	-156.45102	0.0106	0.0085	II
MU106	Maui	Dike	20.83446	-156.59879	1.4900	0.0500	AP
MU109	Maui	Dike	20.83440	-156.59798	1.5500	0.0500	AP
MU111	Maui	Dike	20.83471	-156.59808	1.4500	0.0600	AP
MU113	Maui	Lava Flow	20.78467	-156.54893	1.1000	0.0600	AP
OA003	O'ahu	Flow	21.29434	-157.81123	2.5500	0.0800	AP
OA008	O'ahu	Flow	21.40440	-158.17461	3.7100	0.0600	AP
OA014	O'ahu	Dike	21.51972	-158.22772	3.4900	0.1700	AP
OA015	O'ahu	Flow	21.46033	-158.21154	3.1000	0.0300	AP
OA019	O'ahu	Flow	21.30938	-157.65783	2.8400	0.0600	MP
OA026	O'ahu	Flow	21.29836	-157.65380	2.7700	0.1300	SR
OA028	O'ahu	Flow	21.29907	-157.65273	2.7200	0.0800	AP
OA030	O'ahu	Vent Deposit	21.27831	-157.79929	0.3800	0.1100	O05
OA100	O'ahu	Vent Deposit	21.28628	-157.79791	0.4800	0.0400	O05
OA101	O'ahu	Vent Deposit	21.28521	-157.79900	0.4800	0.0400	O05
OA104	O'ahu	Flow	21.30080	-157.65320	2.1800	0.3500	AP
OA108	O'ahu	Dike	21.30527	-157.65027	2.2500	0.1700	AP
OA114	O'ahu	Dike	21.41002	-157.76354	2.8700	0.0600	AP
OA116	O'ahu	Dike	21.40308	-158.17264	3.7200	0.0500	MP
OA117	O'ahu	Dike	21.40308	-158.17264	3.7200	0.0500	MP
OA123	O'ahu	Sill Margin?	21.40149	-158.17141	2.5900	0.0900	AP
OA124	O'ahu	Dike	21.40168	-158.16927	3.2500	0.0100	MP

laboratory field. Under the IZZI protocol, the order of the in-field and zero-field steps alternates at each temperature step. Under ideal conditions, the ratio of the magnetization lost in a zero-field step to the magnetization gained in an in-field step is the ratio of the ancient field (B_{anc}) to the laboratory field (B_{lab}). For this study, multiple lab fields were used for different specimens, as we observed that the choice of B_{lab} affected whether our specimens passed or failed some of our criteria (see Section 2.3). After each heating, specimens were measured in four positions using the 2G Cryogenic Magnetometer at the Paleomagnetic Laboratory at Scripps Institution of Oceanography.

For sample characterization, a PMC MicroMag 3900 Alternating Gradient Magnetometer was used to measure First Order Reversal Curves (FORCs, Pike et al., 1999) using the xFORC protocol and software of Zhao et al. (2017) on sister specimens from sites used in this study. Sample material from several sites was used to produce doubly polished thin sections. Thermo Fisher Scientific Phenom Desktop Scanning Electron Microscope (SEM) was used to produce Back Scattered Electron (BSE) images, as well as Electron Dispersive X-Ray Spectroscopy (EDS) point observations and maps for identifying the elemental compositions of minerals. These analyses were undertaken at the Scripps Institution of Oceanography Paleomagnetic Laboratory.

2.3 Analysis of Data

To make sure that we have unbiased results, we used two different analysis methods on our data to obtain an estimate of the ancient field. Primarily, we used the Bias Corrected Estimation of Paleointensity (BiCEP) method (Cych et al., 2021) of estimating paleointensities, but we also looked at results using the criteria of Cromwell et al. (2015) (CCRIT). CCRIT are a strict set of selection criteria which exclude many specimens to obtain only results in which we have high confidence. The BiCEP method uses all specimens (without evident alteration), but uses the curvature criterion of Paterson (2011) as a predictor for the bias of the paleointensity yielded by each specimen. This was shown by Tauxe et al. (2022) to produce an unbiased site-level paleointensity estimate while excluding fewer data than the strict CCRIT criteria.

BiCEP assumes that the magnetization records a single field, and thermochemical alteration of the specimen has not occurred. To make certain of this, we used the minimal selection criteria (see Paterson et al., 2014 for definitions and references), DANG<10, DRAT<10. In addition, we use a new parameter, MAD_{Coe}<5 which just uses the zero-field first steps. The set of temperature steps on the Arai plot which maximize the FRAC criterion while passing the MAD_{Coe}, DANG and DRAT criteria. The vast majority of our specimens pass these criteria with ease, and the ones that do not would unambiguously be rejected by almost any other set of criteria.

Site results from BiCEP have a 95% credible interval which is equivalent to the full width of the 2σ interval from traditional selection criteria methods (e.g., CCRIT). We considered a site level result from BiCEP acceptable if it has a credible interval with a full width less than 40% of the median value, or 16 μT, whichever is greater (the original BiCEP A or B criteria of Cych et al., 2021 only include the former criterion). This is equivalent to criteria of $\pm$10% or 4 μT used for the CCRIT at a site level (for a Gaussian distribution, the full width of the 95% credible interval is equal to four standard deviations). An example of BiCEP being used to estimate B_{anc} and its uncertainty for a site is shown in Figure 3.

To compute a time-averaged paleointensity, we used the "Age Hyperparameter Reversible Jump Markov Chain Monte Carlo" (AH-RJMCMC) method (Livermore et al., 2018). This model fits piecewise linear curves to paleointensity data in a probabilistic fashion. The output of the model is a distribution of paleointensity curves, 95% of which lie within a "95% credible" envelope (displayed in Figures 4 and 8). The uncertainties in the paleointensity curves become large during time periods where there are few or no

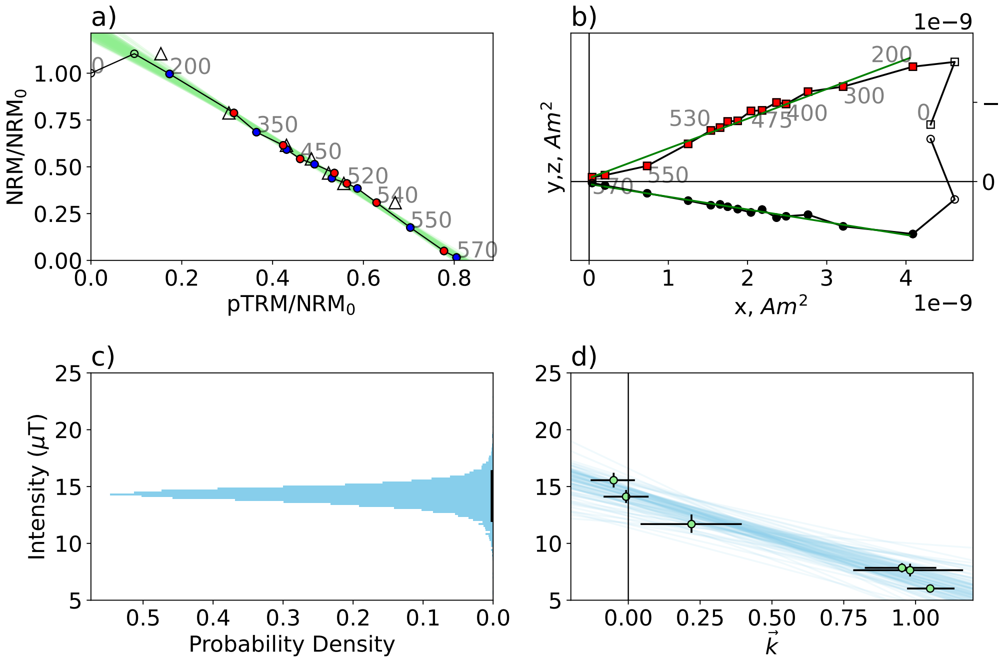

Figure 3. Example of BiCEP being used to obtain a paleointensity for site MU111. a) Arai plot (Nagata et al., 1963) for specimen MU111A05, red dots represent steps where the zero-field measurement was made first, and blue dots represent in-field first steps. Open circles represent temperature steps not used for this analysis. Triangles are pTRM checks and green curves are BiCEP's circular fits to the data. b) Zijderveld plot (Zijderveld, 1967) showing magnetic direction data. Open symbols are steps where the temperature steps were not used. Green line is a principal component analysis fit to the directional data. c) Histogram of possible site mean intensities from BiCEP. d) BiCEP fit showing the predicted relationship (blue lines) between intensity (y axis) and the curvature criterion ($\vec{k}$, x axis) for all six measured specimens from this site.

data. Taking the temporal average of each paleointensity curve produces a distribution of possible time-averaged paleointensities. We discuss the rationale for using this approach in Section 4.3. A similar approach using curve fitting to calculate time-averaged paleointensities was recently used in Bono et al. (2022).

2.4 Age Constraints

We obtained a range of radiometric ages for our samples that span the past 4 Ma. Rocks from 23 of our successful sites were analyzed at the Argon Geochronology lab at Oregon State University (OSU) for age determination. 200-300 μm pieces from each sample were prepared by acid leaching in an ultrasonic bath according to the procedure of Koppers et al. (2000). This was followed by irradiation of the samples in the OSU TRIGA CLICIT nuclear reactor. Samples were then incrementally heated using a defocused CO_2 laser, and the isotopic composition of the released argon was measured using an ARGUS-VI multi-collector mass spectrometer. Eighteen of our ages were calculated using argon-argon (Ar-Ar) plateaus. Sites MU011 and MU036 were calculated using inverse isochron ages, which are typically used when the initial sample contains excess ^{40}Ar. Three ages from sites OA019, OA116 and OA124 were calculated using mini-plateau ages, using less than 50% of the Ar released (Heaton & Koppers, 2019) and site ML001 was calculated using a total fusion age because neither a reliable plateau or isochron age could be calculated. The mini-plateau and total fusion ages should be considered less reliable than the inverse isochron or plateau ages, as these samples could have been affected by argon recoil or loss (Schaen et al., 2021). For sites OA030, OA100 and OA101, we used existing potassium-argon (K-Ar) ages (Ozawa et al., 2005), and on West Maui, existing K-Ar ages (Tagami et al., 2003) were similarly used for sites MU009 and MU013. Mapped scoria cones at sites MU023, MU025 and MU027 have good age constraints over the timescale we are interested in from K-Ar dating and stratigraphic relationships outlined in Sherrod et al. (2003). Finally, sites HW306 and OA026 have their age constrained by stratigraphic relationship with other Ar-Ar dated flows. Ages obtained using the inverse isochron and plateau methods generally yielded consistent results when analysis with both methods was possible. Additionally, our inverse isochron age for site MU011 was highly consistent with the previous K-Ar age obtained by Tagami et al., 2003. A full table of ages is given in Table 1, and plots of the age vs cumulative argon released can be found in Supplementary Figure S1.

3 Results

Results are listed in Table 2. We obtain passing results from 35 sites (Table 2): 31 passed BiCEP and 21 passed CCRIT. Some of the results that pass CCRIT do not pass BiCEP, but those sites that pass both methods exhibit good agreement between one another. Because BiCEP gives a more objective analysis, and because we obtain more passing results with this method, we use only the results that pass BiCEP for the rest of our analyses.

We plot our results versus age in Figure 4. It is apparent that our results support the hypothesis that the more recent field (over the past $\sim$1.5 Ma) is considerably higher than that from 1.5-4 Ma (e.g., Tauxe, 2006), supporting the hypothesis of a potential long period variation in the field strength (Selkin & Tauxe, 2000; Tauxe, 2006; Ziegler et al., 2011). It is also worth noting that in Figure 1, latitudes which have age distributions skewing towards ages older than 1 Ma (e.g., 80°S, 60°N, 0°) tend to have averages that agree with a $\sim$40 ZAm^2 dipole, whereas the majority of latitudes with mostly younger results tend to agree with a 60-70 ZAm^2 dipole moment, so qualitatively our hypothesis that the missing dipole may be caused by temporal sampling seems plausible. However, the data from Antarctica (Asefaw et al., 2021) span the entire last 4 Ma but also have an average field consistent with a 40 ZAm^2 axial dipole strength, so temporal sampling alone does not explain all of the deviation from a GAD field.

The high paleointensity results over the past 1.5 Ma come predominantly from vent deposits (scoria and spatter cones), whereas older results come predominantly from dikes and lava flows. The dikes and lava flows are associated with the early shield building stages of Hawai‘ian volcanoes, whereas the vent deposits are predominantly from the later stages of volcanic construction. The difference in lithology being coupled with a difference in field strength may be concerning, however our young, high field strength results agree well with the average paleointensity from lava flows in the HSDP2 core (Cai et al., 2017; Tauxe & Love, 2003, reanalyzed in Tauxe et al., 2022), shown as grey triangles in Figure 4, although the variance of the HSDP2 data is larger. Additionally, results from several scoria cones yielded fields weaker than 30 μT, including two cones on Moloka‘i older than 1.5 Ma. This leads us to believe that our results from scoria are accurate.

4 Discussion

4.1 Pitfalls of selection criteria

We used the BiCEP method to obtain site level paleointensity estimates, and prefer this over the CCRIT method (and all other sets of selection criteria in use by var-

Table 2. Paleointensity results from specimens in this study which passed BiCEP and CCRIT. n_{pass}: Number of passing specimens. n_{tot}: Total number of specimens. For CCRIT results B_{min} and B_{max} represent the bounds of the 2σ interval, and so a full width of 40% or 16 μT is considered to have passed. The method column represents the preferred paleointensity result (BiCEP) when a site passed both BiCEP and CCRIT

Site	n_{pass}/n_{tot}	B_{min} (μT)	B_{anc} (μT)	B_{max} (μT)	Method
HW306	8/8	30.8	36.8	42.9	BiCEP
ML001	7/7	23.2	31.2	39.2	BiCEP
ML012	6/6	28.1	29.0	30.2	BiCEP
ML015	5/5	5.5	12.0	16.7	BiCEP
MU004	11/11	39.3	42.3	45.5	BiCEP
MU009	6/6	31.1	36.6	42.4	BiCEP
MU011	5/9	19.2	26.5	33.8	CCRIT
MU012	6/6	31.8	34.6	37.6	BiCEP
MU013	8/8	14.8	19.2	23.8	BiCEP
MU023	8/8	26.1	31.0	35.6	BiCEP
MU025	7/7	33.9	42.1	50.2	BiCEP
MU027	6/6	19.7	24.7	30.7	CCRIT
MU031	10/10	34.6	40.4	46.0	BiCEP
MU036	9/9	10.4	10.9	11.4	BiCEP
MU106	10/12	22.1	28.8	35.0	BiCEP
MU109	7/7	15.9	18.8	21.9	BiCEP
MU111	6/6	12.1	14.3	16.2	BiCEP
MU113	8/8	38.1	43.7	49.7	BiCEP
OA003	11/11	26.9	29.2	31.3	BiCEP
OA008	4/4	14.9	20.2	26.2	BiCEP
OA014	10/12	10.3	13.0	15.6	BiCEP
OA015	8/8	35.3	39.7	44.5	BiCEP
OA019	15/15	20.5	22.9	25.3	BiCEP
OA026	8/8	12.5	15.0	17.4	BiCEP
OA028	8/8	29.4	33.1	36.8	BiCEP
OA030	16/16	45.6	48.9	52.2	BiCEP
OA100	6/12	50.0	51.0	52.0	CCRIT
OA101	9/9	37.3	43.0	48.3	BiCEP
OA104	3/8	15.8	17.6	19.3	CCRIT
OA108	8/8	13.2	19.5	25.5	BiCEP
OA114	6/6	21.8	25.3	30.2	BiCEP
OA116	8/8	21.7	24.9	28.2	BiCEP
OA117	5/5	19.2	23.7	28.1	BiCEP
OA123	6/8	10.3	13.8	19.0	BiCEP
OA124	7/7	33.8	36.8	40.2	BiCEP

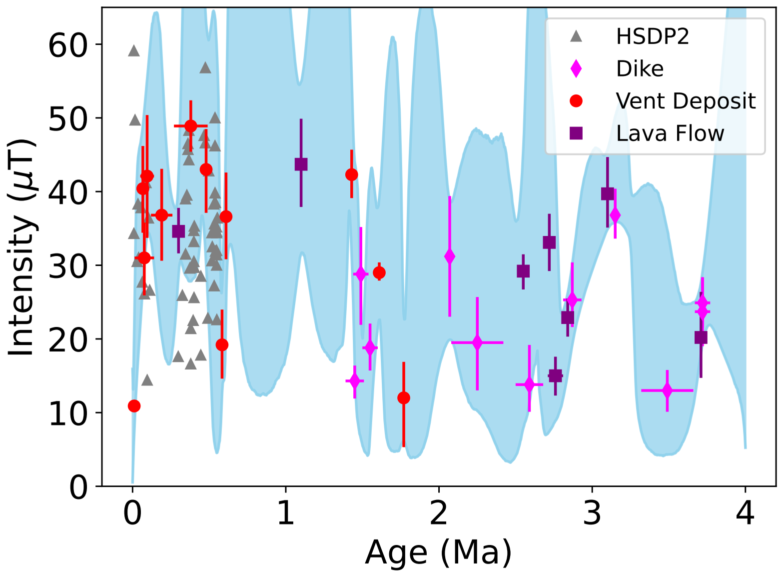

Figure 4. Paleointensity and age estimates from this study using the BiCEP method from lava flows (purple squares), scoria cones (red circles) and dike margins (pink diamonds). Error bars represent the 95% credible interval for intensity estimates, and the 2σ interval for age estimates. Grey triangles are other Hawai'ian results from the HSDP2 core (Cai et al., 2017; Tauxe & Love, 2003, Tauxe et al., 2022), which have a similar distribution over this time period to our results. Blue envelope represents the 95% credible interval for the AH-RJMCMC model (Livermore et al., 2018) fit to the data (see Section 4.3).

ious authors) as BiCEP produces many more site level results than CCRIT. Often, BiCEP passed sites where specimens failed the FRAC criterion of CCRIT, which specifies that a large proportion of the total magnetization of the specimen is needed to make a paleointensity estimate. BiCEP accounts for the uncertainty in curvature (and therefore bias), introduced by using only part of a specimen's Arai plot for a paleointensity estimate. This can be seen in Figure 3a, where specimen MU111A05 fails CCRIT due to low FRAC, but using a smaller part of the Arai plot translates to only a small increase in the uncertainty in curvature, shown by the green curves fit to the data.

In addition to the FRAC criterion in CCRIT, we identify cases in which criteria may reject a specimen if it has an ancient field much lower than the lab field. The MAD criterion may be exceeded if the laboratory magnetization acquired in an in-field step is not fully removed during a zero-field step, a consequence of a "high temperature pTRM tail" (Dunlop & Özdemir, 2000). This behavior is very noticeable in IZZI experiments (Figure 5), as the in-field first steps are more strongly affected by this effect. This leads to a zig-zag appearance in the Zijderveld plot. The sizes of these tails are dependent on both the magnitude of the lab field, and the effect the tails have on MAD is dependent on the angle between lab and ancient field. If we call this angle θ, then the perpendicular part of the tails will be controlled by $B_{lab}\sin\theta$. If we assume no other sources of deflection to the MAD angle, the equation for the effect is:

$$\tan(\mathrm{MAD}) \propto \frac{B_{lab}}{B_{anc}} \sin\theta. \quad (1)$$

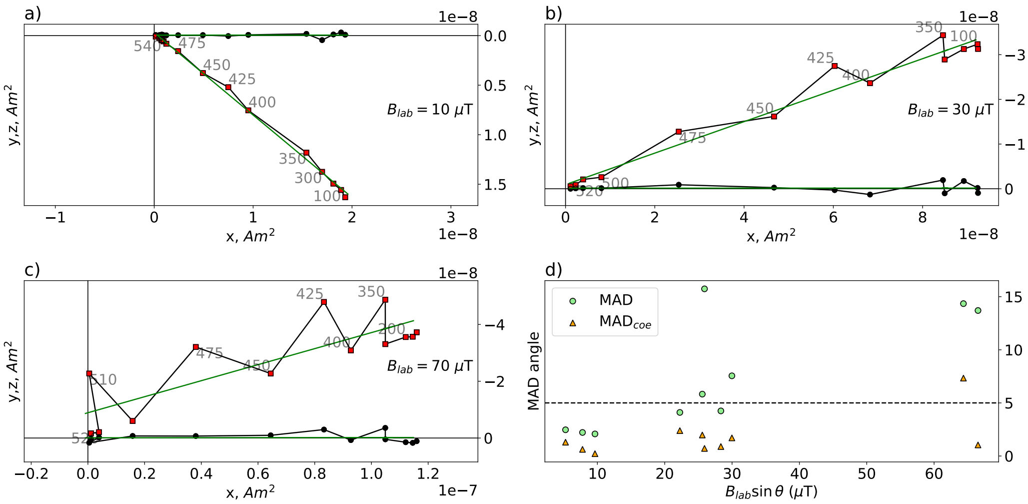

Figure 5. a)-c) Zijderveld plots of specimens from site OA014, showing zig-zagging behavior that progressively increases with lab field and d) Scatter plot showing the relationship between the MAD criterion, and the magnitude and angle of the lab field for all ten fully demagnetized specimens from this site. Paleointensity experiments were performed laboratory fields of a) a 10 μT, b) 30 μT and c) 70 μT. d) MAD (green circles) angle against the strength of the component of the lab field perpendicular to the ancient field direction (calculated by the PCA of the zero-field first steps). Orange triangles are the MAD of the zero-field first steps only ($\mathrm{MAD_{Coe}}$). Horizontal dashed line represents the selection criterion (5) used in this study. Using $\mathrm{MAD_{Coe}}$ improves, though does not completely eliminate, the lab-field dependence of MAD. All MADs were calculated using temperature steps from 400-600°C to avoid any potential viscous remanent magnetization (VRM).

This equation demonstrates that in the same lab field, sites with low ancient fields will be preferentially rejected with higher MAD, and sites with high ancient fields will be preferentially accepted.

To counteract the lab field-dependent effects, we used 10, 30 and 70 μT fields in our studies, which captures the range of the ancient field. At some sites with low estimated B_{anc}, there was an observably higher pass rate in lower fields. An example of this for site OA014 is illustrated in Figure 5. To treat specimens magnetized in different fields fairly, it is tempting to come up with a criterion for MAD which is dependent on Equation 1. However, effects that we may be using MAD to look for (e.g., two component magnetizations) will not be dependent on the lab field, and so we suggest calculating MAD for exclusively the zero-field first or "Coe" type steps (Coe, 1967). Although pTRM tails may still be present in these steps, they will be significantly reduced in in-field first steps. We call a MAD calculated using these steps MAD_{Coe} and how it compares to MAD for site OA014 is shown in Figure 5d. The use of MAD_{Coe} significantly reduces the lab field-dependent effects, but does not eliminate them entirely. Because pTRMs scale with the lab field used, there may be other unrecognized pTRM dependent effects. We recommend using a range of lab fields in paleointensity studies as the most robust way of compensating for these effects.

In addition to the lab field dependence of directional statistics, criteria which depend on pTRM checks (such as DRAT used in this study) have their own problems. Thermochemical alteration of magnetic material with blocking temperatures higher than the heating temperature can produce curved Arai plots with passing pTRM checks, as has been suggested by e.g. Wang and Kent (2021) and McClelland and Briden (1996). Additionally, although pTRM checks are used to detect alteration, they themselves may be caused by multi-domain carriers (Wang et al., 2013). Fortunately, the source of curvature is unlikely to matter for the BiCEP method, as it has been shown to yield accurate results when applied naively to a large test dataset, including passed and failed pTRM checks with no selection (Cych et al., 2021). However, the term "thermochemical alteration" describes a wide range of processes, and so in this study we cautiously excluded temperature steps where pTRM checks failed. More work is required to better understand thermochemical alteration processes and separate them from domain-state related behavior, for which the RESET method of Wang and Kent (2021) may be useful.

4.2 Sample Characterization

We have demonstrated our ability to obtain high quality paleointensity results from our samples using the BiCEP method. However, it is not clear what the primary carriers of the magnetization are for these samples, particularly for samples from vent deposits, which are relatively unstudied in the paleointensity literature. To attempt to characterize the domain state of our samples, we obtained First Order Reversal Curves (FORCs, Pike et al., 1999) for selected material from sites which passed BiCEP (and from some which failed). For this analysis we used sister specimens from the same samples for which the paleointensity results were acquired. FORCs are a qualitative way of assessing the domain state of a specimen using its hysteresis properties, and they can be decomposed into transient (tFORC), induced (iFORC) and remanent (remFORC) components using to the protocol of Zhao et al. (2017). Specimens which contain "Single-Domain" (SD) grains which are ideal for the paleointensity experiment will have FORCs with a central ridge of positive values along the H_a=-H_b axis (see e.g., Figure 6a). Specimens with higher numbers of non SD grains will have FORCs which have a spread along the H_a=H_b axis. The iFORC which represents the induced part of the magnetization displays a pattern of three distinct "lobes" (e.g., Figure 6b,f) for a sample containing SD grains, whereas it may display four "lobes" or be extremely noisy for samples containing non-SD grains. The tFORC represents "transient hysteresis" which occurs in non-SD grains; specimens with just noise on the tFORC (e.g., Figure 6c) are most likely to be single domain.

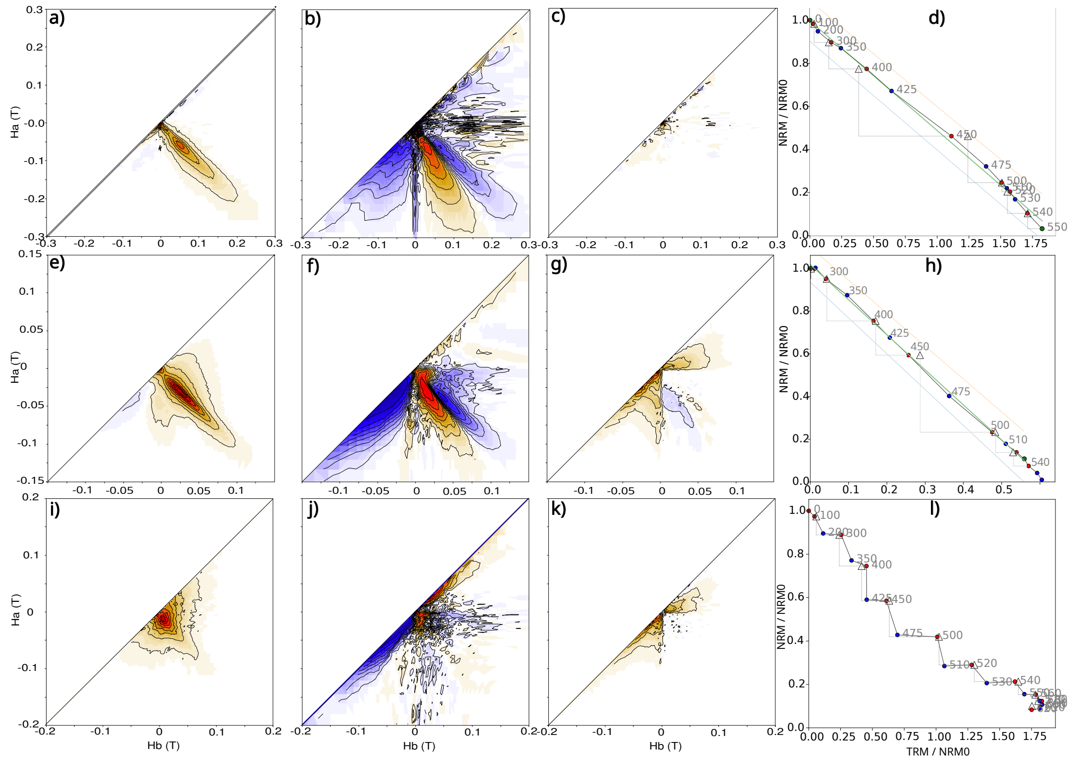

Figure 6. First Order Reversal Curves (FORCs) a),e),i), iFORCs b),f),j), and tForcs c),g),k) calculated using the xFORC protocol (Zhao et al., 2017). All FORCs calculated using a smoothing factor of 2 and a non-linear color scale of 1, except for iFORCs which were calculated using a smoothing factor of 3 and a non-linear color scale of 10. Arai plots are plotted in d),h),l). FORCs use sister specimens from two sites that yielded passing results: OA030 (top row), OA014 (center row) and a site which did not pass CCRIT or BiCEP, HW305 (bottom row). Sites which yielded specimens with linear Arai plots tend to have an elongated central ridge and have 3 lobes in the iFORC (top and center rows), whereas sites with curved Arai plots tend to have more spread along the $H_a = H_b$ direction and have extremely noisy iFORCs with little information.

Examples of FORCs and Arai plots for different samples are displayed in Figure 6. The FORC interpretations generally agree with the paleointensity experimental results. FORCs obtained from dike samples have pronounced central ridges and three lobes in the iFORC if visible, and effectively no tFORC (Figure 6a-d). These samples generally had Arai plots which were straight lines, but sometimes underwent thermochemical alteration at high temperatures. Samples from lava flows and vent deposits had central ridges, with small amounts of transient hysteresis and spreading along the $H_a = H_b$ axis. These samples still have linear Arai plots, and often have three lobes present in the iFORC, which suggests that the majority of carriers in these specimens are single domain (see Figure 6e-h). An example from a relatively coarse grained lava flow is given in Figure 6i-l. Samples like these had highly curved or zig-zagging Arai plots (Figure 6l) and generally had no central ridge and lots of spreading along the $H_a = H_b$ axis (Figure 6i). These samples had pronounced tFORCs (Figure 6k), and only noise in the iFORCs away from the H_a axis (Figure 6j), observations which are consistent with the curved and zig-zagging Arai plots.

We also obtained Back Scattered Electron (BSE) images using an Scanning Electron Microscope (SEM), and Electron Dispersive X-Ray Spectroscopy (EDS) element

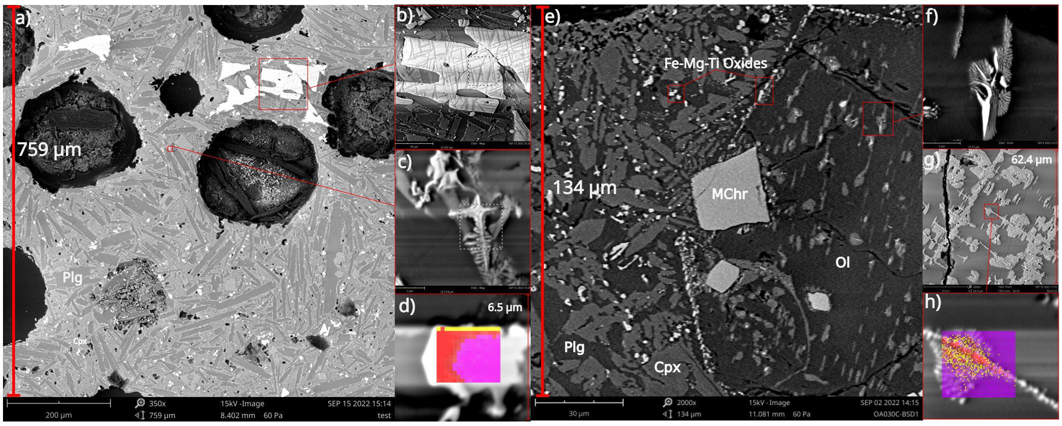

Figure 7. Back Scattered Electron (BSE) images and Electron Dispersive X-Ray Spectroscopy (EDS) maps of sister specimens from selected samples used in this study. Red text gives vertical field of view (FOV) for each image. a) BSE image of sample ML015A, a scoria vent deposit. b) Zoomed in image of large oxide in a), showing Fe-Ti exsolution textures. c) Zoomed in image of small oxide in a), showing elongate skeletal/cruciform structure. d) EDS element map of a typical oxide from another scoria vent deposit, ML012A, showing heterogeneous composition in the Iron-Titanium oxides. The atomic content of Si is shown in yellow, Fe in red, and Ti in pink. e) BSE image of sample OA030A, an agglutinated basanite vent deposit. f) Close up of high temperature alteration texture in olivine phenocryst. g) The same texture present in sample MU012A, a breccia from the bottom of a basanite lava flow. h) Close up of this texture with EDS element map. Colors are the same as d), with purple representing Mg. Note that the light colors in the BSE image represent an iron rich phase (interpreted as magnetite), which is surrounded by a phase richer in silicon than the surrounding olivine, interpreted as enstatite. Dominant mineral phases written on a) and e): Plg: plagioclase feldspar, Cpx: clinopyroxene, Ol: olivine, MChr: chrome spinel. Horizontal banding present in b),c),d),f),h) is an artifact of charging the sample that occurs in the SEM's EDS element mapping mode.

maps to identify iron oxides in several thin sections taken from our samples. Several pictures from these analyses are displayed in Figure 7 and further images of dike samples are displayed in supplementary Figure S2. Dike samples we analyzed contained no visible iron oxides in the glass, and almost no iron oxides in the groundmass. This is consistent with our FORCs and Arai plots (Figure 6a-d), which are indicative of this specimen containing a predominance of single domain grains, which are 10s of nm in scale and not resolvable by the SEM used in this analysis. By contrast, samples from vent deposits contained numerous micron-scale iron bearing oxides in the groundmass, and in some cases, larger iron oxides on the scales of 100s of microns (Figure 7a-d), size ranges where we would expect the grains to yield curved Arai plots. Many of these grains have elongated "cruciform" textures (Figure 7c) or have heterogeneous compositions (Figure 7a,d). One possibility is that these textures may persist to smaller scales, causing the larger grains to behave like assemblages of smaller, single domain, grains, due to their elongation or having smaller magnetic subregions separated by nonmagnetic lamellae. Another possibility is that these large grains do not contribute to the remanence. However, the lava flows and vent deposits have much higher NRM moments than the dikes, with mass normalized NRMs on the order of 10^{-2} to 10^{-3} Am^2/kg, as opposed to the dikes which have moments on the order of 10^{-4} to 10^{-5} Am^2/kg.

Two thin sections from sites MU012 and OA030 have numerous olivine grains which exhibit an unusual texture, as displayed in Figure 7e-h. This texture has been observed previously (Ejima et al., 2017; Blondes et al., 2012) and is interpreted as being caused by oxidation of olivine at temperatures above 800°C, which causes breakdown into an iron oxide (magnetite or hematite depending on formation conditions) and enstatite (see Figure 7h and figure caption). The temperature of the oxidation means that the samples were oxidized prior to gaining a magnetization, which means the NRM is a primary TRM acquired during cooling. Oxidation of this kind seems to typically occur in fire fountaining strombolian type eruptions (e.g., Del Moro et al., 2013) where the lavas remain at high temperatures in an oxidizing environment for a while (e.g., 950 °C for 24-48 hours as per Haggerty & Baker, 1967). OA030 is an agglutinated basanitic vent deposit, agreeing with this oxidative environment, whereas the MU012 sample was taken from breccia/clinkers in an a'ā lava flow (rough fragmented pieces at the bottom of the flow), which may also undergo high temperature oxidation although the source is less clear.

Both sites with evidence for high temperature oxidation of olivines had highly linear Arai plots (see Figure 6h), with 16/16 specimens passing the strict CCRIT criteria for OA030, and 6/6 passing for MU012. Additionally a sample from OA030 has a FORC indicative of single-domain to single-vortex domain state, with a central ridge and three lobes in the iFORC (see Figure 6, middle row). This indicates that the oxides formed by this breakdown may have extremely desirable properties for paleointensity experiments. Similar to the smaller oxides found in our other vent deposits (Figure 7c), the elongation and finger-like structures present in these oxides could also explain their ideal behavior in the paleointensity experiment. These thin sections also contained numerous micron scale iron-titanium-magnesium oxides (interpreted as magnesioferrite) in the groundmass and around the outside of the olivine grains (Figure 7e), but because the majority of the remanence unblocks between 400 and 600°C (see Figure 6d), we believe that magnetite is the dominant remanence carrier in these specimens.

Despite the large iron oxides observed in vent deposits and lava flows from this study, we conclude that these lithologies provide a good source for paleointensity estimates, as they have a high success rate relative to our other lithologies owing to their strikingly linear Arai plots (see Figure 6, top row). Site MU113 provides further evidence for this, as material sampled from the inside of a lava tube gave an identical result to material sampled from a scoriaceous bomb entrained in the same flow. There are other reasons to favour these types of lithologies: The formation of these samples in an oxic environment at high temperature may help prevent thermochemical alteration during the pa-

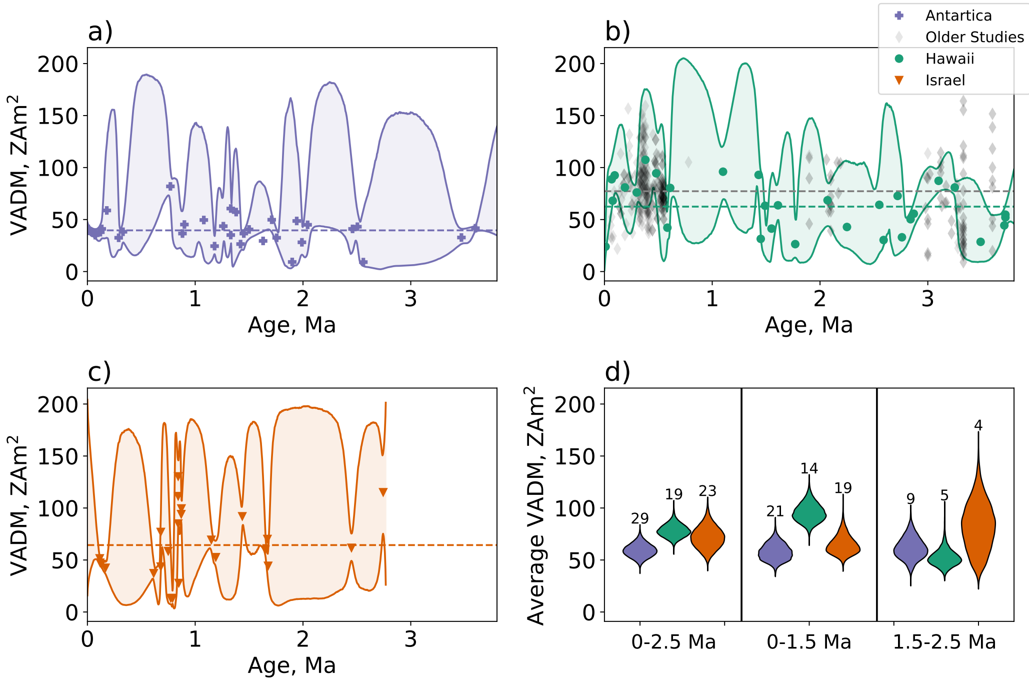

Figure 8. a) - c) Plots of VADM against age (symbols), and 95% credible envelopes for AH-RJMCMC models (Livermore et al., 2018) (shaded areas) for studies from a) Antarctica (purple plus symbols), b) Hawai'i (green dots), and c) Israel (orange triangles). Horizontal dashed lines are the average VADM of all paleointensity estimates (symbols) for each plot. In b), all unfiltered data in the MagIC database from Hawai'i aged between 50 ka and 3.8 Ma are plotted as grey diamonds, and the average VADM from these data are plotted as a grey horizontal line. d) Violin plots showing the distribution of averaged VADMs over different time periods, numbers refer to the number of paleointensity within these temporal ranges, although data outside these ranges may also contribute to these averages. Data from Hawai'i have a significantly higher average VADM than in Israel and Antarctica over the past 1.5 Ma, which is reflected in the averages from 0-2.5 Ma. Average VADMs for data older than 1.5 Ma appears to agree for all three locations.

leointensity experiment, and fresh scoria is also easy to come by in Hawai'i, as many scoria cones are quarried. However, most preserved vent deposits are typically formed during the later stages of Hawai'ian volcanism, and consequently we have no results from scoria older than 2 Ma.

4.3 Temporal Distributions of Intensity

Mismatch between the observed distribution of paleointensities with latitude and the expected distribution for a GAD field (Figure 1a) could potentially be caused by inconsistencies in treatment of data among different paleointensity studies. To compare the time-averaged field from our model to data from different latitudes, we reanalyzed results from recent paleomagnetic studies in Northern Israel (Tauxe et al., 2022) and Antarctica (Asefaw et al., 2021) using the BiCEP method and the same criteria used for the Hawai'i samples. Tables of results from these re-analyses can be found in the Supporting Information. Each of these studies yielded passing sites with results spanning the past 2.5 Ma. For direct comparisons between locations, we convert each paleointensity result to a Virtual Axial Dipole Moment (VADM) which is the moment of the geocentric dipole (measured in ZAm^2) that would yield the observed paleointensity at a given latitude. Our average VADM for Hawai'i is 62.4 ZAm^2, which is similar to the 64.2 ZAm^2 value from Israel, but is significantly higher than the average in Antarctica (39.6 ZAm^2). Plots of VADMs with age for each location are shown in Figures 8a)-c), with average VADMs plotted as horizontal dashed lines. In Figure 8b we also plot all the data from Hawai'i in the MagIC database from this time interval in grey. The unfiltered data have a significantly higher variance than our data, and the weaker field seen prior to 1.5 Ma in our data is not apparent in the unfiltered Hawai'ian data, which have an average VADM of 77.2 ZAm^2. These differences could occur because more field variation is being captured by the larger dataset, or because the unfiltered data have more variance due to inconsistency in their analysis (for example, preferentially taking the low temperature steps in a potentially sagging Arai plot). Despite the consistency in analysis of our data, the average VADM in Hawai'i and Israel is still very different to that found in Antarctica, indicating that inconsistency in analyses and biased paleointensities caused by Arai plot curvature are not the source of this mismatch.

Taking an average VADM of the entire age range of our data may not be representative of the time-averaged field, because our data have different temporal distributions, with no data in Israel older than 2.75 Ma. In Hawai'i, this average does not capture the change in average field strength seen at 1.5 Ma, and in Israel, we have many paleointensity data which record a strong field and come from a small range of time around 850 ka B.P. Because this time interval is oversampled, it will bias our average VADM towards these higher values. For this reason, we used the the AH-RJMCMC method (see Section 2.3), which produces a set of possible paleointensity curves for each locality. We took the average value of each curve over the past 2.5 Ma, and converted these averages to VADMs. At times where there are many paleointensity data, the curves produced by the AH-RJMCMC have high precision, but only locally, so the time period is not over-represented in the average. At times when there are few data, the model uncertainties become very large and revert to a uniform prior distribution(which we set as 0-220 ZAm^2), indicating that we do not have enough data to resolve any inconsistencies in the VADM between localities at those times.

The models produced by the AH-RJMCMC analysis are shown in Figure 8a-c, and the distributions of the time-averaged VADMs for each locality are plotted on the violin plots in Figure 8d. Using this methodology, it is apparent that the time-averaged VADMs over the last 1.5 Ma from Hawai'i and Antarctica are indeed not consistent with each other, but the time-averaged VADM in Israel could be compatible with either of the other latitudes. However, there is not enough evidence to confirm a difference in the temporal average between Hawai'i and Antarctica from 1.5-2.5 Ma, with the average VADMs appearing consistent. This implies that poor temporal sampling is not the reason for inconsistent paleointensities at different latitudes, but that some form of genuine non-dipolar field behavior that causes higher fields in Hawai'i than Antarctica at least since 1.5 Ma. More paleointensity studies with high quality paleointensity data at different latitudes (especially from the southern hemisphere) are needed to better understand the sources of this non-dipolar behavior.

5 Conclusions

In this paper, we obtained 31 high quality paleointensity results from dikes, lava flow tops and vent deposits collected in the Hawai'ian islands, with ages ranging from 0-4 Ma. We demonstrate a methodology for obtaining accurate time-averaged paleointensities, with uncertainties which allow direct comparison between paleointensity studies at different latitudes. The use of BiCEP allows for consistent comparison of results between different studies, and using the methodology of Livermore et al. (2018) allows us to obtain a time-averaged intensity, with uncertainty, which accounts for the temporal distribution of our paleointensity. Because these robust statistical approaches are used for calculating time-averaged paleointensities, we are able to exclude the hypotheses that inconsistency of our time-averaged VADMs is due to either biased paleointensity data, or inconsistent temporal sampling of paleointensities.

Applying the new methodology to data from the Hawai'ian islands, we find that the time-averaged paleointensity in Hawai'i over the past 1.5 Ma was higher than during the period from 1.5-4 Ma. Comparing results from paleointensity studies at three latitudes, we find that this period of high paleointensity is not recorded in rocks from Antarctica or Israel. We reiterate the conclusion of other recent papers (e.g., Tauxe et al., 2022) that the Earth's magnetic field averaged over the past 1.5 Ma does not conform to a Geocentric Axial Dipole. Further time averages at a greater range of latitudes and times will be needed to obtain better estimates of the structure of this time-averaged field.

Our results also indicate that vent deposits containing scoria, and olivine bearing rocks which are oxidized at high temperatures are potentially good lithologies for obtaining high quality paleointensity estimates, with higher success rates in the paleointensity experiment. Specimens from these lithologies have strong magnetizations and tend to alter less in paleointensity experiments. Additionally, these deposits are frequently quarried, allowing for easy access to fresh material in the field. Despite their useful properties in paleointensity experiments, and their single-domain like FORCs, the size of iron oxides in these samples when viewed under a microscope is orders of magnitude larger than would be expected for single domain grains. Further study of the magnetic carriers in these samples should be undertaken to understand why they have such ideal rock magnetic properties.

Open Research

All data and interpretations are available at `https://earthref.org/MagIC/19614/9208acad-0f62-4d9e-b265-4c8907d40eb7` and will be made available in the MagIC database at `http://earthref.org/MagIC/19614` on acceptance of this paper. Python notebooks for producing figures can be found at `https://github.com/bcych/hawaiian_paleointensity` and the release version associated with this paper can be found at the Zenodo repository `https://doi.org/10.5281/zenodo.7921097` (Cych, 2023).

Acknowledgments

This work was partially supported by EAR1827263 to LT and EAR1520788 to GC. We would like to thank Huapei Wang and one anonymous reviewer for their helpful reviews of the manuscript. We would additionally like to thank the Hawai'i Department of Land and Natural Resources' Forestry and Wildlife Program for issuing sampling permits in West Maui, and Moloka'i Ranch Ltd. and Moloka'i Land Trust for allowing us to sample on their land. We are grateful for comments from Cathy Constable and Jeffery Gee which improved the manuscript. Finally we would like to thank the late Jasper Konter for his help in the field and hospitality during our field work on Oahu. He will be missed.

References

Asefaw, H., Tauxe, L., Koppers, A. A. P., & Staudigel, H. (2021). Four-dimensional paleomagnetic dataset: Plio-Pleistocene paleodirection and paleointensity results from the Erebus Volcanic Province, Antarctica. *J. Geophys. Res. Solid Earth*, *126*(2), e2020JB020834. doi: 10.1029/2020JB020834

Blondes, M. S., Brandon, M. T., Reiners, P. W., Page, F. Z., & Kita, N. T. (2012). Generation of forsteritic olivine (Fo99·8) by subsolidus oxidation in basaltic flows. *J. Petrol.*, *53*(5), 971–984. doi: 10.1093/petrology/egs006

Bono, R. K., Paterson, G. A., & Biggin, A. J. (2022). MCADAM: A Continuous

Paleomagnetic Dipole Moment Model for at Least 3.7 Billion Years. *Geophys. Res. Lett.*, *49*(21), e2022GL100898. doi: 10.1029/2022GL100898

Cai, S., Tauxe, L., & Cromwell, G. (2017). Paleointensity from subaerial basaltic glasses from the second Hawaii Scientific Drilling Project (HSDP2) core and implications for possible bias in data from lava flow interiors. *J. Geophys. Res. Solid Earth*, *122*(11), 8664–8674. doi: 10.1002/2017JB014683

Coe, R. S. (1967). The determination of paleo-intensities of the earth's magnetic field with emphasis on mechanisms which could cause non-ideal behavior in thellier's method. *J. Geomag. Geoelectr.*, *19*, 157–178.

Cromwell, G., Johnson, C. L., Tauxe, L., Constable, C. G., & Jarboe, N. A. (2018). PSV10: A global data set for 0–10 Ma time-averaged field and paleosecular variation studies. *Geochem. Geophys. Geosyst.*, *19*(5), 1533–1558. doi: 10.1002/2017GC007318

Cromwell, G., Tauxe, L., & Halldórsson, S. A. (2015). New paleointensity results from rapidly cooled Icelandic lavas: Implications for Arctic geomagnetic field strength. *J. Geophys. Res. Solid Earth*, *120*(5), 2913–2934. doi: 10.1002/2014JB011828

Cromwell, G., Tauxe, L., Staudigel, H., Constable, C. G., Koppers, A. A. P., & Pedersen, R.-B. (2013). In search of long-term hemispheric asymmetry in the geomagnetic field: Results from high northern latitudes. *Geochem. Geophys. Geosyst.*, *14*(8), 3234–3249. doi: 10.1002/ggge.20174

Cych, B. (2023). *bcych/hawaiian_paleointensity: Initial version for publication.* Zenodo. Retrieved from `https://doi.org/10.5281/zenodo.7921097` doi: 10.5281/zenodo.7921097

Cych, B., Morzfeld, M., & Tauxe, L. (2021). Bias Corrected Estimation of Paleointensity (BiCEP): An improved methodology for obtaining paleointensity estimates. *Geochem. Geophys. Geosyst.*, *22*(8), e2021GC009755. doi: 10.1029/2021GC009755

Del Moro, S., Renzulli, A., Landi, P., La Felice, S., & Rosi, M. (2013). Unusual lapilli tuff ejecta erupted at Stromboli during the 15 March 2007 explosion shed light on the nature and thermal state of rocks forming the crater system of the volcano. *J. Volcanol. Geotherm. Res.*, *254*, 37–52. doi: 10.1016/j.jvolgeores.2012.12.017

Dunlop, D., & Özdemir, O. (2000). Effect of grain size and domain state on thermal demagnetization tails. *Geophys. Res. Lett.*, *27*, 1311-1314.

Dunlop, D., & Özdemir, O. (2001). Beyond Néel's theories: thermal demagnetization of narrow-band partial thermoremanent magnetization. *Phys. Earth Planet. Int.*, *126*, 43-57.

Ejima, T., Yoneda, M., Akasaka, M., Ohfuji, H., Kon, Y., Nagashima, M., & Nakamuta, Y. (2017). Precipitates within olivine phenocrysts in oxidized andesitic scoria from Kasayama volcano, Hagi, Japan. *J. Mineral. Petrol. Sci.*, *112*(3), 116–126. doi: 10.2465/jmps.161219

Haggerty, S. E., & Baker, I. (1967). The alteration of olivine in basaltic and associated lavas. *Contrib. Mineral. Petrol.*, *16*(3), 233–257. doi: 10.1007/BF00371094

Heaton, D. E., & Koppers, A. A. P. (2019). High-Resolution 40Ar/39Ar Geochronology of the Louisville Seamounts IODP Expedition 330 Drill Sites: Implications for the Duration of Hot Spot-related Volcanism and Age Progressions. *Geochem. Geophys. Geosyst.*, *20*(8), 4073–4102. doi: 10.1029/2018GC007759

Koppers, A. A. P., Staudigel, H., & Wijbrans, J. R. (2000). Dating crystalline groundmass separates of altered Cretaceous seamount basalts by the 40Ar/39Ar incremental heating technique. *Chem. Geol.*, *166*(1), 139–158. doi: 10.1016/S0009-2541(99)00188-6

Krása, D., Heunemann, C., Leonhardt, R., & Petersen, N. (2003). Experimental procedure to detect multidomain remanence during Thellier–Thellier experiments. *Phys. Chem Earth (A/B/C)*, *28*(16), 681 - 687. (Paleo, Rock and Environmental Magnetism 2002) doi: 10.1016/S1474-7065(03)00122-0

Lawrence, K. P., Tauxe, L., Staudigel, H., Constable, C., Koppers, A., McIntosh, W. C., & Johnson, C. L. (2009). Paleomagnetic field properties near the southern hemisphere tangent cylinder. *Geochem. Geophys. Geosyst.*, *10*, Q01005. doi: doi:10.1029/2008GC002072

Levi, S. (1977). The effect of magnetite particle size on paleointensity determinations of the geomagnetic field. *Phys. Earth Planet. Inter.*, *13*(4), 245–259. doi: 10.1016/0031-9201(77)90107-8

Livermore, P. W., Fournier, A., Gallet, Y., & Bodin, T. (2018). Transdimensional inference of archeomagnetic intensity change. *Geophys. J. Int.*, *215*(3), 2008–2034. doi: 10.1093/gji/ggy383

McClelland, E., & Briden, J. C. (1996). An improved methodology for Thellier-type paleointensity determination in igneous rocks and its usefulness for verifying primary thermoremanence. *J. Geophys. Res. Solid Earth*, *101*(B10), 21995–22013. doi: 10.1029/96JB02113

Muxworthy, A. R. (2017). Considerations for latitudinal time-averaged-field palaeointensity analysis of the last five million years. *Front. Earth Sci.*, *0*. doi: 10.3389/feart.2017.00079

Nagata, T., Arai, Y., & Momose, K. (1963). Secular variation of the geomagnetic total force during the last 5000 years. *J. Geophys. Res.*, *68*, 5277-5282.

Néel, L. (1949). Théorie du traînage magnétique des ferromagnétiques en grains fins avec applications aux terres cuites. *Ann. géophys.*, *5*, 99–136.

Ozawa, A., Tagami, T., & Garcia, M. O. (2005). Unspiked K–Ar dating of the Honolulu rejuvenated and Koʻolau shield volcanism on Oʻahu, Hawaiʻi. *Earth Planet. Sci. Lett.*, *232*(1), 1–11. doi: 10.1016/j.epsl.2005.01.021

Paterson, G. A. (2011). A simple test for the presence of multidomain behavior during paleointensity experiments. *J. Geophys. Res. Solid Earth*, *116*(B10). doi: 10.1029/2011JB008369

Paterson, G. A., Tauxe, L., Biggin, A., Shaar, R., & Jonestrask, L. (2014). On improving the selection of Thellier-type paleointensity data. *Geochemistry Geophysics Geosystems*, *15*(4). doi: 10.1002/2013GC005135

Pike, C., Roberts, A., & Verosub, K. (1999). Characterizing interactions in fine magnetic particle systems using first order reversal curves. *J. Appl. Phys.*, *85*, 6660-6667.

Schaen, A. J., Jicha, B. R., Hodges, K. V., Vermeesch, P., Stelten, M. E., Mercer, C. M., ... Singer, B. S. (2021). Interpreting and reporting 40Ar/39Ar geochronologic data. *GSA Bulletin*, *133*(3-4), 461–487. doi: 10.1130/B35560.1

Selkin, P., & Tauxe, L. (2000). Long-term variations in paleointensity. *Phil. Trans. Roy. Soc. Lond.*, *358*, 1065-1088.

Shaar, R., Bechar, S., Finkelstein, I., Gallet, Y., Martine, M., Ebert, Y., ... Gonen, L. (2020). Synchronizing archaeomagnetic field intensity records in the Levant between the 23^{rd} and 15^{th} cennturies BCE: chronological and methodological implications. *Geochemistry Geophysics Geosystems*, *21*, e2020GC009251. doi: 10.1029/2020GC009251

Shcherbakov, V. P., Khokhlov, A. V., & Sycheva, N. K. (2019). Analysis of the hypothesis of a Giant Gaussian Process as a means for describing secular variations of the geomagnetic field vector. *Izv. Phys. Solid Earth*, *55*(1), 182–194. doi: 10.1134/S1069351319010099

Sherrod, D. R., Nishimitsu, Y., & Tagami, T. (2003). New K-Ar ages and the geologic evidence against rejuvenated-stage volcanism at Haleakala, East Maui, a postshield-stage volcano of the Hawaiian island chain. *GSA Bulletin*, *115*(6), 683–694. doi: 10.1130/0016-7606(2003)115⟨0683:NKAATG⟩2.0.CO;2

Sherrod, D. R., Sinton, J. M., Watkins, S. E., & Brunt, K. M. (2007). Geologic map of the State of Hawaii. *US geological survey open-file report*, *1089*, 83.

Tagami, T., Nishimitsu, Y., & Sherrod, D. R. (2003). Rejuvenated-stage volcanism after 0.6-m.y. quiescence at West Maui volcano, Hawaii: New evidence from K–Ar ages and chemistry of Lahaina Volcanics. *J. Volcanol. Geotherm. Res.*, *120*(3), 207–214. doi: 10.1016/S0377-0273(02)00385-2

Tauxe, L. (2006). Long-term trends in paleointensity: The contribution of DSDP/ODP submarine basaltic glass collections. *Physics of the Earth and Planetary Interiors*, *156*(3-4), 223-241.

Tauxe, L., Asefaw, H., Behar, N., Koppers, A. A. P., & Shaar, R. (2022). Paleointensity Estimates from the Pleistocene of Northern Israel: Implications for hemispheric asymmetry in the time-averaged field. *Geochem. Geophys. Geosyst.*, *n/a*(n/a), e2022GC010473. doi: 10.1029/2022GC010473

Tauxe, L., & Love, J. J. (2003). Paleointensity in Hawaiian Scientific Drilling Project Hole (HSDP2): Results from submarine basaltic glass. *Geochem. Geophys. Geosyst.*, *4*(2). doi: 10.1029/2001GC000276

Tauxe, L., Santos, C. N., Cych, B., Zhao, X., Roberts, A. P., Nagy, L., & Williams, W. (2021). Understanding nonideal paleointensity recording in igneous rocks: Insights from aging experiments on lava samples and the causes and consequences of “fragile” curvature in Arai plots. *Geochem. Geophys. Geosyst.*, *22*(1), e2020GC009423. doi: 10.1029/2020GC009423

Tauxe, L., & Staudigel, H. (2004). Strength of the geomagnetic field in the Cretaceous Normal Superchron: New data from submarine basaltic glass of the Troodos Ophiolite. *Geochem. Geophys. Geosyst.*, *5*(2). doi: 10.1029/2003GC000635

Wang, H., & Kent, D. V. (2021). RESET: A Method to Monitor Thermoremanent Alteration in Thellier-Series Paleointensity Experiments. *Geophys. Res. Lett.*, *48*(5), e2020GL091617. doi: 10.1029/2020GL091617

Wang, H., Kent, D. V., & Jackson, M. J. (2013). Evidence for abundant isolated magnetic nanoparticles at the Paleocene–Eocene boundary. *Proc. Natl. Acad. Sci. U.S.A.*, *110*(2), 425–430. doi: 10.1073/pnas.1205308110

Wilson, R. L. (1970). Permanent aspects of the Earth’s non-dipole magnetic field over Upper Tertiary times. *Geophys. J. Int.*, *19*(4), 417–437. doi: 10.1111/j.1365-246X.1970.tb06056.x

Yu, Y., Tauxe, L., & Genevey, A. (2004). Toward an optimal geomagnetic field intensity determination technique. *Geochem. Geophys. Geosyst.*, *5*(2). doi: 10.1029/2003GC000630

Zhao, X., Roberts, A. P., Heslop, D., Paterson, G. A., Li, Y., & Li, J. (2017). Magnetic domain state diagnosis using hysteresis reversal curves. *J. Geophys. Res. Solid Earth*, *122*(7), 4767–4789. doi: 10.1002/2016JB013683

Ziegler, L., Constable, C., Johnson, C. L., & Tauxe, L. (2011). PADM2M: a penalized maximum likelihood model of the 0-2 Ma paleomagneitic axial dipole moment. *Geophys. J. Int.*, *184*, 1069-1089.

Zijderveld, J. D. A. (1967). *A.C. demagnetization of rocks: Analysis of results.* Chapman and Hall.